REVIEWS

Anisotropic optical and electric properties of β-gallium oxide

Yonghui Zhang† and Fei Xing†

School of Physics and Optoelectronic Engineering, Shandong University of Technology, Zibo 255000, China

Abstract: The anisotropic properties and applications of β-gallium oxide (β-Ga$_2$O$_3$) are comprehensively reviewed. All the anisotropic properties are essentially resulted from the anisotropic crystal structure. The process flow of how to exfoliate nanoflakes from bulk material is introduced. Anisotropic optical properties, including optical bandgap, Raman and photoluminescence characters are comprehensively reviewed. Three measurement configurations of angle-resolved polarized Raman spectra (ARPRS) are reviewed, with Raman intensity formulas calculated with Raman tensor elements. The method to obtain the Raman tensor elements of phonon modes through experimental fitting is also introduced. In addition, the anisotropy in electron mobility and affinity are discussed. The applications, especially polarization photodetectors, based on β-Ga$_2$O$_3$ were summarized comprehensively. Three kinds of polarization detection mechanisms based on material dichroism, 1D morphology and metal-grids are discussed in-depth. This review paper provides a framework for anisotropic optical and electric properties of β-Ga$_2$O$_3$, as well as the applications based on these characters, and is expected to lead to a wider discussion on this topic.

Key words: gallium oxide; anisotropic; dichroism; polarization; monoclinic

1. Introduction

β-gallium oxide (β-Ga$_2$O$_3$) is an ultra-wide bandgap (UWBG) semiconductor with superior electronic and optoelectronic properties. For one thing, due to the wide direct optical bandgap of 4.9 eV, β-Ga$_2$O$_3$ is widely used in deep-ultraviolet (DUV) photodetectors[1, 2]. Multifarious device configurations, including PN junction[3], PIN junction[4], heterojunction[5], Schottky photodiodes[6], MSM devices[7], avalanche photodiodes[8] and phototransistors[9, 10], have been reported based on β-Ga$_2$O$_3$ wafers, thin-films and nanostructures. High photoresponsivity of more than 4000 A/W[10] and response speed less than 12 ns[11] were realized. For another thing, since β-Ga$_2$O$_3$ features high breakdown field strength of 8 MV/cm and Baliga's figure of merit (BFOM) of 3400, which is four times larger than GaN and 4H-SiC, it is also a promising candidate in power electronics and high-voltage devices[12]. High breakdown voltage of more than 3000 V has been reported in β-Ga$_2$O$_3$ Schottky diodes with lateral field-plate structure[13]. Up to 8.03 kV ultra-high breakdown voltage was achieved in field-plated lateral β-Ga$_2$O$_3$ MOSFETs[14]. Currently, DUV photodetector and power electronics are the two major application research interests of β-Ga$_2$O$_3$, while still there are some other applications, such as gas sensors[15] and X-ray detectors[16].

Given the ubiquitous applications, β-Ga$_2$O$_3$ has gained much attention, especially, in recent ten years. Besides, the low symmetry of crystal structure renders β-Ga$_2$O$_3$ exceeding anisotropic properties. In this review, we will emphasize on the unique anisotropic properties and applications of β-Ga$_2$O$_3$.

Correspondence to: Y H Zhang, yhzhang@sdut.edu.cn; F Xing, xingfei@sdut.edu.cn

2. Anisotropic crystal structure of β-Ga$_2$O$_3$

β-Ga$_2$O$_3$ is actually a reborn material, and related research can be traced back to 1960s[17, 18]. However, it is until recent ten years, especially from 2010, that β-Ga$_2$O$_3$ received growing attention from the area of power electronics and DUV optical devices. β-Ga$_2$O$_3$ has based-centered monoclinic lattice structure, which belongs to C2/m space group (space group number: 12), with inherent structure anisotropy[19]. Fig. 1(a) shows one unit-cell of β-Ga$_2$O$_3$, with an exceptional long base vector **a** of 12.21 Å, relatively short base vectors **b** of 3.04 Å and **c** of 5.80 Å. The α angle between x and y axes as well as the γ angle between y and z axes is right angle, while the β angle between x and z axes is 103.83°. There are two kinds of Ga^{3+} ions and three kinds of O^{2-} ions in β-Ga$_2$O$_3$ crystal. As shown in Fig. 1(b), one kind of Ga^{3+}, named Ga Ⅰ, occupies the distorted Ga$_Ⅰ$O$_4$ tetrahedral site, while the other kind of Ga^{3+}, named Ga Ⅱ, occupies the distorted Ga$_Ⅱ$O$_6$ octahedral site. Both Ga Ⅰ and Ga Ⅱ ions are equal in quantity and both the Ga$_Ⅰ$O$_4$ tetrahedrons and Ga$_Ⅱ$O$_6$ octahedrons are aligned along [010] direction[20]. Band structure calculation[21] suggests that the anisotropic arrangement of Ga$_Ⅰ$O$_4$ tetrahedrons lead to the anisotropic electric and optoelectronic properties as will be discussed later in the following sections.

The anisotropic lattice structure of β-Ga$_2$O$_3$ renders the possibility of cleavage of thin flakes along x axis (the [100] direction) or z axis (the [001] direction)[22], since atoms are relatively weaker bonded in these directions compared to those in y axis (the [010] direction) where atoms are tightly bonded through the chains of Ga$_Ⅰ$O$_4$ tetrahedrons and Ga$_Ⅱ$O$_6$ octahedrons. As shown in Fig. 1(b), the Ga$_Ⅱ$O$_6$ octahedrons share edges to form double chains, furthermore the double chains are bonded together via Ga$_Ⅰ$O$_4$ tetrahedrons. All the three atom chains are parallel to y axis, leading to the intense covalent bonds along y axis[23]. Due to the huge difference in bond-
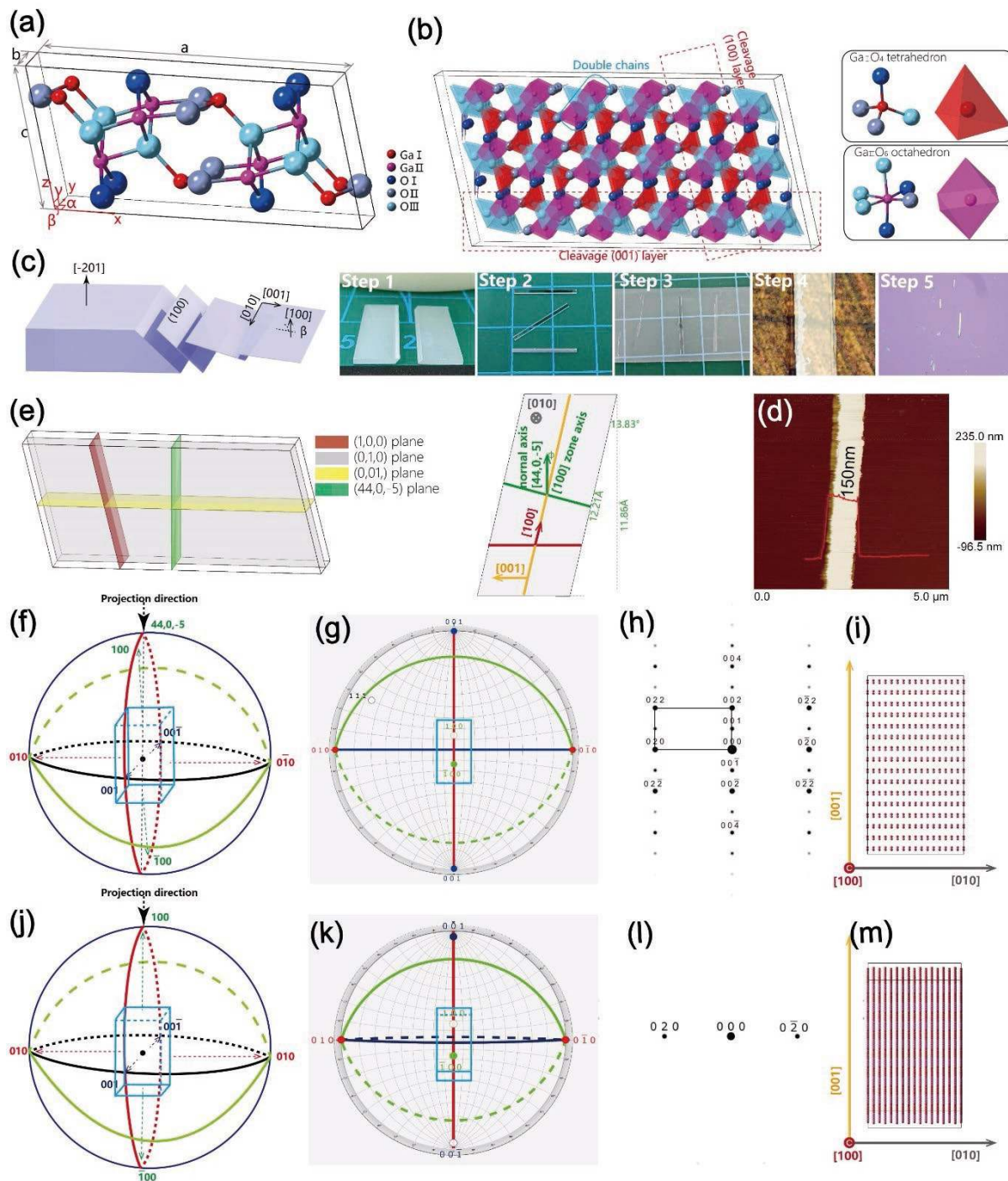
Fig. 1. (Color online) Anisotropic cystal structure of β-Ga$_2$O$_3$. (a) Unit cell of β-Ga$_2$O$_3$. (b) 2 × 2 cells with Ga$_I$O$_4$ tetrahedral and Ga$_{II}$O$_6$ octahedral chains. (c) Process flow of mechanical exfoliation of β-Ga$_2$O$_3$ nanobelts. (d) AFM result of one typical β-Ga$_2$O$_3$ nanobelt. (e) Lattice frame of β-Ga$_2$O$_3$. (f) Stereographic projection, (g) projection plane, (h) electron diffraction pattern and (i) projection view of β-Ga$_2$O$_3$ along [44, 0, −5] direction. (j) Stereographic projection, (k) projection plane, (l) electron diffraction pattern and (m) projection view of β-Ga$_2$O$_3$ along [100] direction.

ing strength between directions parallel and perpendicular to [010] direction, β-Ga$_2$O$_3$ can be easily exfoliated in (100) and (001) planes. In Fig. 1(c), the typical process flow of mechanical exfoliation is depicted. Step 1: the [−201] oriented β-Ga$_2$O$_3$ single crystal is manually broken into two parts, with cleavage plane of (100). Step 2: single-crystal slices of less than one millimeter thick can be peeled off from the bulk material. Step 3: the thickness of the slices can be reduced to few microns by riving with adhesive tape. Step 4: further reduce the thickness of β-Ga$_2$O$_3$ nanobelts to the thickness of tens to hundreds of nanometers. Step 5: dry-transfer the

nanobelts onto substrate. The thickness of a typical nanobelt is measured with atomic force microscope (AFM) to be 150 nm [Fig. 1(d)].

For exfoliated β-Ga$_2$O$_3$ nanomaterials, (100) plane is the crystal plane to be used in many applications and characterizations. For clarity in analysis and calculation, it should be pointed out that, the [100] direction is not the normal direction of (100) plane[24] [Fig. 1(e)]. In addition, to accurately analyze the crystal structure, researchers should notice the difference between the concept of zone axis, in the crystal lattice, and the normal axis, in the laboratory coordinate system[25].

For (010) and (001) planes, it is easy to determine the zone axis [uvw] to be [100], according to the Weiss zone law,

$$u = k_1l_1 - k_2l_2,$$
$$v = l_1h_2 - l_2h_1,$$
$$w = h_1k_2 - h_2k_1,$$
(1)

where (h_1, k_1, l_1) = (010) and (h_2, k_2, l_2) = (001). To figure out the normal axis of the (100) plane, that is the incident direction of optical characterizations, such as Raman scattering, photoluminescence and photodetector device applications, the included angles of crystal planes shall be calculated using

$$\cos\phi = \frac{d_1d_2}{\sin^2\beta}\left[\frac{h_1h_2}{a^2} + \frac{k_1k_2\sin^2\beta}{b^2} + \frac{l_1l_2}{c^2} - \frac{(l_1h_2 + l_2h_1)\cos\beta}{ac}\right],$$
(2)

where φ is the included angle between (h_1, k_1, l_1) and (h_2, k_2, l_2) crystal planes, d_1 and d_2 are crystal plane spacing of (h_1, k_1, l_1) and (h_2, k_2, l_2), a, b, c, β are the lattice constants as defined above. Assuming the index of the normal direction to be [h, k, l] and the interplane space to be d, for the two planes of (h, k, l) and (010),

$$\cos 90° = 0 = \frac{dd_{(010)}}{\sin^2\beta}\left[0 + \frac{k\sin^2\beta}{b^2} + 0 - 0\right],$$
(3)

for the two planes of (h, k, l) and (010),

$$\cos 90° = 0 = \frac{dd_{(001)}}{\sin^2\beta}\left[0 + 0 + \frac{l}{c^2} - \frac{h\cos\beta}{ac}\right],$$
(4)

for the two planes of (h, k, l) and (100),

$$\cos 13.83° = \frac{dd_{(100)}}{\sin^2\beta}\left[\frac{h}{a^2} + 0 + 0 - \frac{l\cos\beta}{ac}\right].$$
(5)

For monoclinic crystal structure, the crystal plane spacing d can be obtained via

$$\frac{1}{d^2} = \frac{h^2}{a^2\sin^2\beta} + \frac{k^2}{b^2} + \frac{l^2}{c^2\sin^2\beta} - \frac{2lh\cos\beta}{ca\sin^2\beta}.$$
(6)

The orientation index [h, k, l] is calculated to be [44, 0, −5] by solving the above Eqs. (3)–(6).

If the projection direction is perpendicular to (100) plane [Fig. 1(f)], that is the typically vertical direction in the laboratory coordinate, the atoms are staggered arranged along [001] direction and cyclically arranged along [010] direction, as can be seen in Fig. 1(i). In the process of electron diffraction, electrons would be diffracted by atomic cores in the [44, 0, −5] plane [Fig. 1(g)], and diffraction pattern can be acquired as in Fig. 1(h). In another case, if the projection direction is along [100] direction [Fig. 1(j)], the atoms are arranged unordered along [001] and periodically along [010] direction from the view direction [Fig. 1(m)]. Accordingly, electrons are diffracted by atomic cores in the [100] plane [Fig. 1(k)], and a different diffraction pattern would appear as in Fig. 1(l).

Since high-quality β-Ga$_2$O$_3$ nanomaterials could be obtained via mechanically exfoliation, researchers have done intensive studies to apply β-Ga$_2$O$_3$ nanoflakes in various applications. Sooyeoun *et al*. reported metal-semiconductor-metal

(MSM) photodetector by exfoliating [100] oriented β-Ga$_2$O$_3$ micro-flakes from bulk single crystal[24]. Li *et al*. reported large drain current β-Ga$_2$O$_3$ field-effect transistors with mechanically exfoliated β-Ga$_2$O$_3$ flakes[26]. The reported device performances using exfoliated β-Ga$_2$O$_3$ flakes are generally superior than others using bottom-up synthesis approaches, as the flakes inherit the high crystalline quality from the bulk single crystal. The innovativeness of exfoliation method is quite surprising since, unlike graphene and MoS$_2$, β-Ga$_2$O$_3$ is not a conventional 2D layered material. The feasibility of layer-by-layer exfoliation results from the strong covalent bonding along [010] direction and relatively weak bonding along [100] and [001] directions. That is why β-Ga$_2$O$_3$ is often referred to as quasi-two-dimensional material[26–30]. The anisotropic crystal structure of β-Ga$_2$O$_3$ leads to the unique optical and electrical properties as will be discussed in the following sections.

3. Anisotropic optical properties

3.1. Anisotropic bandgap

Due to the high anisotropic crystal structure, β-Ga$_2$O$_3$ features highly anisotropic optical properties, among which the anisotropic optical bandgap is the most in-depth studied one. The optical absorption edges for $E//b$ and $E//c$ polarized light were 4.79 and 4.52 eV, respectively, according to Ueda's report[31]. It was also found that the rate of the band gap widening with increasing carrier concentration was much larger for $E//b$ than $E//c$. It should be noted that, technically, β-Ga$_2$O$_3$ is an indirect-bandgap material with the minimum gap between the Γ point in conduction band minimum (CBM) and the M point in valance band maximum (VBM). However, since the valance band is quite flat and the M point is only a few meV higher than the Γ point in the valance band, the inter-band transition behavior is essentially that of a direct-bandgap material[32]. According to the first principle calculation, the CBM of β-Ga$_2$O$_3$, which mainly constituted by Ga 4s orbitals, is isotropic, while the VBM, constituted by oxygen 2p orbitals, is largely anisotropic[33, 34] [Fig. 2(a)]. The valance band minimum, which occurs just off the M point and is only 0.03 eV higher than at Γ, is set to zero on the energy axis. The absorption onsets of $E//a$, $E//b$ and $E//c$ polarized light are shown in Fig. 2(b). From the results for polarization parallel to the three crystallographic axes, one can draw the conclusion that the lowest absorption edge is along $E//c$, followed by the close onset of $E//a$, while $E//b$ gives the obvious highest onset value. The absorption coefficient is plotted in Tauc form with exponent of 2, indicating that researchers treated β-Ga$_2$O$_3$ as a direct bandgap material although its bandgap is indirect in nature. It is clear to see that there is approximately 0.5 eV difference in the optical bandgap between the cases of $E//b$ and $E//c$. Chen *et al*. reported the polarized transmittance characteristics of β-Ga$_2$O$_3$ single crystal, and revealed the transitions from valance subbands to the CBM which is tuned between 4.54 to 4.76 eV for 0° to 90° polarization between $E//c$ and $E//b$[35] [Fig. 2(c)]. The angle resolved transmittance verifies that the band-to-band transitions obey well the selection rules in terms of the valence-band splitting in the β-Ga$_2$O$_3$ monoclinic crystal band structure. The angle dependence transmittance power at 4.6 eV can be expressed as $T(\xi) = T_{E//b}\sin^2(\xi) + T_{E//c}\cos^2(\xi)$, where the in-plane polarization angle ξ is defined as the angle between
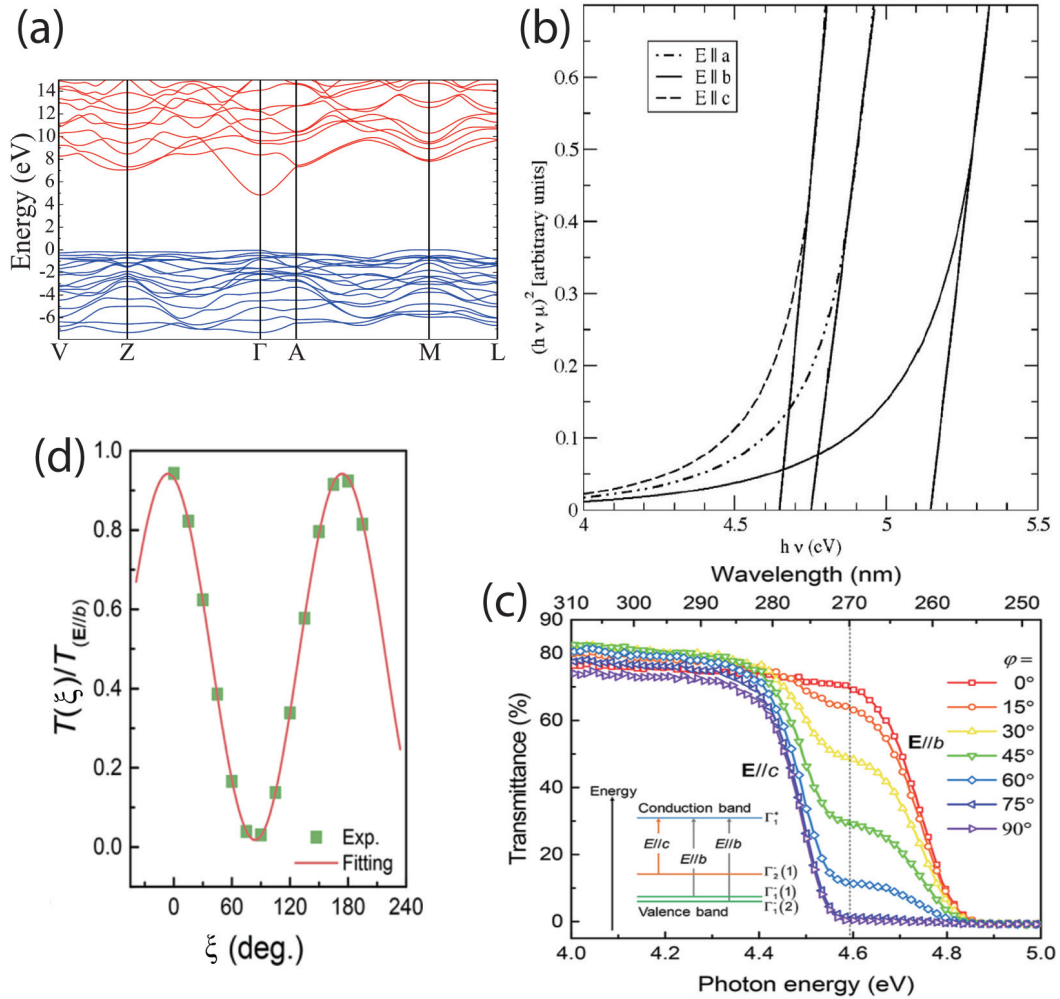
Fig. 2. (Color online) Anisotropic optical bandgap of β-Ga$_2$O$_3$. (a) Band structure for β-Ga$_2$O$_3$ calculated using the primitive unit cell of base-centered monoclinic[32]. Copyright 2010 by AIP publishing. (b) Tauc plot of the absorption coefficient, showing the polarization-dependent onsets[33]. Copyright 2016 by IOP publishing. (c) Polarized transmittance spectra of a β-Ga$_2$O$_3$ (100) single crystal and (d) transmittance magnitude with respect to $E//b$ as a function of in-plane polarization angle[35]. Copyright 2019 by American Chemical Society.

Table 1.   Anisotropic bandgaps from literatures.

Ref.	Morphology	Synthesis method	Characterization	$E_g(a)$ (eV)	$E_g(b)$ (eV)	$E_g(c)$ (eV)
[34]	–	–	Calculation	2.307	2.975	2.478
[33]	Bulk	EFG	Absorption	4.57	4.72	4.54
[36]	Bulk	EFG	Transmittance	4.58	4.73	4.48
[35]	Bulk	EGG	Transmittance	–	4.76	4.53
[37]	Bulk	FZ	Transmittance	–	4.86	4.56
[31]	Bulk	FZ	Transmittance	–	4.79	4.52

the b axis and the electric field vector E and $T_{E//b}$ and $T_{E//c}$ represent the transmittance magnitudes for the cases of $\xi = 0°$ and 90° at 4.6 eV, respectively [Fig. 2(d)].

Yamaguchi reported[34] the irreducible representations of the eigen-functions of band levels at Γ point in 2004, in which, the CBM state at Γ belongs to Γ_1^+, while VBM, the 55th and 56th states belong to Γ_2^-. The transition of polarized dipoles along x ($E//a$) and z ($E//c$) directions are allowed by the selection rule of 56th and 55th state (at Γ_2^- point) to 57th state (at Γ_1^+ point), respectively. While the transition of polarized dipoles along y ($E//b$) direction is allowed by the selection rule of 51st and 52nd states (at Γ_1^- point) to 57th state. According to the group theory, the direct transition from Γ_1^+ and Γ_2^+ are forbidden. Therefore, the optical bandgap is

expected to be related merely to the VBM at Γ_1^- and Γ_2^- which is about 0.67 eV lower beneath it, disregarding the existence of Γ_1^+ and Γ_2^+ states. The drop difference from the 56th to the 52nd states are 0.67 eV, which is in good consistency with the anisotropic bandgap difference from other papers listed in Table 1. It should be noted that there is distinct bandgap order for the three polarization directions, that is $E||c < E||a < E||b$. Theoretical calculation indicates the energy ordering is actually due to suppression of the transition matrix elements of three top valence bands[33].

3.2. Raman scattering and Raman tensor

Raman scattering technique is generally employed in condensed matter physics for nondestructive-probing of crystal's phonon mode and lattice dynamics. Since the behavior of elec-
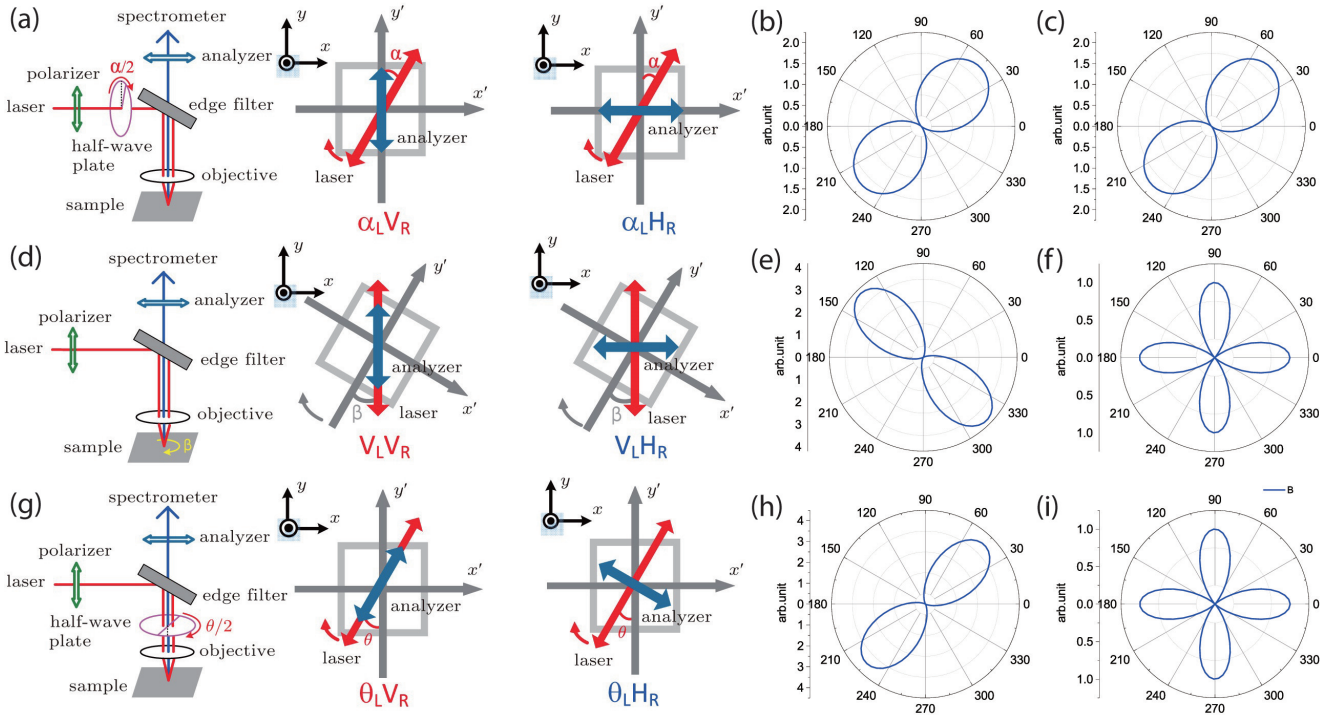
Fig. 3. (Color online) Schematic diagrams of three typical polarization configurations for angle-resolved polarized Raman spectroscopy[25]. Copyright 2017 by IOP publishing. (a) The schematic diagram of type 1 configuration. Polar plots of the Raman intensity when the analyzer is set along (b) vertical and (c) horizontal directions. (d) The schematic diagram of type 2 configuration. Polar plots of the Raman intensity when the analyzer is set along (e) vertical and (f) horizontal directions. The schematic diagram of type 3 configuration. Polar plots of the Raman intensity when the analyzer is (h) vertical and (i) horizontal to the incident laser direction.

trons, phonons and their coupling influence the optical and electrical properties of β-Ga$_2$O$_3$, Raman spectroscopy has been proven to be an effective and non-destructive testing tool. In addition, due to the high anisotropy of β-Ga$_2$O$_3$ single crystal, angle-resolved polarized Raman spectroscopy (ARPRS) is utilized in studying the anisotropic physical properties. ARPRS features periodically varied Raman intensity for each of the vibration modes, which is directly related to the corresponding Raman tensor elements. Despite the same physical connotation, ARPRS measurement could be operated in several configurations, thus lead to different results and analyzing processes. Liu *et al.* summarized three typical ARPRS measurement configurations as illustrated in Fig. 3[25].

Type 1: Vary the angle of the incident light, while keep the sample steady

This configuration, as shown in Fig. 3(a), is the most commonly used one as it is time-saving and easy-to-operate. At the beginning, the polarization angle of the incident light is in consistence with y axis. By simply rotating the fast axis of the half-wave plate, which is placed in the incident laser beam path, with an angle of $\alpha/2$, the polarization angle of the incident light rotates with an angle of α from the y axis. Since the objective sample is stationary, the angle between the polarization direction and the sample could be modulated accordingly. The intensity of the ARPRS spectra can be fitted with Raman tensor through the equation[25]

$$I \propto \sum_j |e_R \cdot R_j \cdot e_L|^2, \quad (7)$$

where e_R and e_L are the unit polarization vector of the Raman signal and the incident beam, R_j is a 3×3 Raman tensor. The overall Raman intensity is the sum of the polarized Raman signal, along e_R, which is twisted by the Raman tensor from e_L. Generally, the Raman tensor is composed with nine independent numbers, for instance, a to g.

$$R_j = \begin{pmatrix} a & b & c \\ d & e & f \\ g & h & i \end{pmatrix}. \quad (8)$$

From Bilbao Crystallographic Server[38], researchers can find the characteristic Raman tensors of materials according to their space group. For β-Ga$_2$O$_3$, space group C2/m (No. 12), under non-resonant condition, the Raman tensors can be simplified in the form[39]

$$A_g : R_j = \begin{pmatrix} a & d & 0 \\ d & b & 0 \\ 0 & 0 & c \end{pmatrix}; \quad B_g : R_j = \begin{pmatrix} 0 & 0 & e \\ 0 & 0 & f \\ e & f & 0 \end{pmatrix}. \quad (9)$$

The polarization of the incident laser, e_L, can be expressed in the form $e_L = (\sin\alpha \ \cos\alpha \ 0)$, where α is the angle between the polarization direction and the y' axis of the laboratory coordinate as shown in Fig. 3(a). The polarization direction of the analyzer is fixed either parallel or vertical to the y' axis with unit vector $e_R = (010)$ and (100), respectively. The overall Raman intensity in this configuration can be calculated via

$$I = \left| (0 \ 1 \ 0) \begin{pmatrix} a & d & 0 \\ d & b & 0 \\ 0 & 0 & c \end{pmatrix} \begin{pmatrix} \sin\alpha \\ \cos\alpha \\ 0 \end{pmatrix} \right|^2 = |d\sin\alpha + b\cos\alpha|^2. \quad (10)$$

If the polarization direction of the analyzer is set along x', that is $e_R = (100)$, the overall Raman intensity in this configuration can be calculated via

$$I = \left| (1\ 0\ 0) \begin{pmatrix} a & d & 0 \\ d & b & 0 \\ 0 & 0 & c \end{pmatrix} \begin{pmatrix} \sin\alpha \\ \cos\alpha \\ 0 \end{pmatrix} \right|^2 = |a\sin\alpha + d\cos\alpha|^2.$$

(11)

The polar plots of β-Ga$_2$O$_3$ ARPRS in this configuration with $e_R = (010)$ and $e_R = (100)$ are shown in Figs. 3(b) and 3(c), respectively. The Raman tensor elements can be acquired by fitting the ARPRS intensity using Eqs. (10) and (11).

Type 2: Rotate sample while keep the incident laser unchanged

The second measurement configuration, as shown in Fig. 3(d), is to rotate the sample while keep the polarization direction of the incident laser unchanged. In this case, the unit polarization vector e_R and e_L is fixed, and the Raman tensor R_j is modified as R_j is defined in crystal coordinates which is rotated in this configuration. The converted Raman tensor R_j' can be expressed as

$$R_j' = M \cdot R_j \cdot M^T,$$

(12)

$$M = \begin{pmatrix} \cos\beta & \sin\beta & 0 \\ -\sin\beta & \cos\beta & 0 \\ 0 & 0 & 1 \end{pmatrix},$$

(13)

where M is a rotating matrix, and β is the angle between the crystal coordinate and laboratory coordinates.

For the case that both the incident laser and the analyzer polarized along y' axis, the intensity of the Raman signal could be calculated via

$$I = \sum_j \left| e_R \cdot M \cdot R_j \cdot M^T \cdot e_L \right|^2 = \left| (0\ 1\ 0) \begin{pmatrix} \cos\beta & \sin\beta & 0 \\ -\sin\beta & \cos\beta & 0 \\ 0 & 0 & 1 \end{pmatrix} \begin{pmatrix} a & d & 0 \\ d & b & 0 \\ 0 & 0 & c \end{pmatrix} \begin{pmatrix} \cos\beta & -\sin\beta & 0 \\ \sin\beta & \cos\beta & 0 \\ 0 & 0 & 1 \end{pmatrix} \begin{pmatrix} 0 \\ 1 \\ 0 \end{pmatrix} \right|^2$$

$$= \left| a\sin^2\beta + b\cos^2\beta - 2d\sin\beta\cos\beta \right|^2.$$

(14)

For the case that the incident laser polarized along y' axis while the analyzer along the x' axis, the intensity of the Raman signal could be calculated via

$$I = \sum_j \left| e_R \cdot M \cdot R_j \cdot M^T \cdot e_L \right|^2 = \left| (1\ 0\ 0) \begin{pmatrix} \cos\beta & \sin\beta & 0 \\ -\sin\beta & \cos\beta & 0 \\ 0 & 0 & 1 \end{pmatrix} \begin{pmatrix} a & d & 0 \\ d & b & 0 \\ 0 & 0 & c \end{pmatrix} \begin{pmatrix} \cos\beta & -\sin\beta & 0 \\ \sin\beta & \cos\beta & 0 \\ 0 & 0 & 1 \end{pmatrix} \begin{pmatrix} 0 \\ 1 \\ 0 \end{pmatrix} \right|^2$$

$$= \left| d(\cos^2\beta - \sin^2\beta) + (b - a)\sin\beta\cos\beta \right|^2.$$

(15)

The polar plots of β-Ga$_2$O$_3$ in this configuration with $e_R = (010)$ and $e_R = (100)$ are shown in Figs. 3(e) and 3(f), respectively.

Type 3: Vary e_R and e_L simultaneously

The third measurement configuration, as shown in Fig. 3(g), is to vary e_R and e_L simultaneously by adjusting the half-wave plate inserted in the optical path between Raman filter and microscope objective. Jones matrix[40] $J_{\lambda/2}$ is involved to quantify the influence of optical devices on polarized light.

$$J_{\lambda/2} = \begin{pmatrix} -\cos\theta & \sin\theta & 0 \\ \sin\theta & \cos\theta & 0 \\ 0 & 0 & 0 \end{pmatrix}.$$

(16)

The polarization e_L of the incident laser is modified by the half-wave plate via $e_L' = J_{\lambda/2} \cdot e_L$, and e_R via $e_R' = e_R \cdot J_{\lambda/2}$. The overall Raman intensity in this configuration can be calculated with

$$I = \sum_j \left| e_R \cdot J \cdot R_j \cdot J \cdot e_L \right|^2.$$

(17)

For analyzer polarized along y' axis, the intensity can be calculated via

$$I = \sum_j \left| e_R \cdot J \cdot R_j \cdot J \cdot e_L \right|^2 = \left| (0\ 1\ 0) \cdot \begin{pmatrix} -\cos\theta & \sin\theta & 0 \\ \sin\theta & \cos\theta & 0 \\ 0 & 0 & 0 \end{pmatrix} \cdot \begin{pmatrix} a & d & 0 \\ d & b & 0 \\ 0 & 0 & c \end{pmatrix} \cdot \begin{pmatrix} -\cos\theta & \sin\theta & 0 \\ \sin\theta & \cos\theta & 0 \\ 0 & 0 & 0 \end{pmatrix} \cdot \begin{pmatrix} 0 \\ 1 \\ 0 \end{pmatrix} \right|^2$$

$$= \left| a\sin^2\theta + b\cos^2\theta + 2d\sin\theta\cos\theta \right|^2.$$

(18)

For analyzer that polarized along x' axis, the intensity can be calculated via

$$I = \sum_j |e_R \cdot J \cdot R_j \cdot J \cdot e_L|^2 = \left| \begin{pmatrix} 1 & 0 & 0 \end{pmatrix} \cdot \begin{pmatrix} -\cos\theta & \sin\theta & 0 \\ \sin\theta & \cos\theta & 0 \\ 0 & 0 & 0 \end{pmatrix} \cdot \begin{pmatrix} a & d & 0 \\ d & b & 0 \\ 0 & 0 & c \end{pmatrix} \cdot \begin{pmatrix} -\cos\theta & \sin\theta & 0 \\ \sin\theta & \cos\theta & 0 \\ 0 & 0 & 0 \end{pmatrix} \cdot \begin{pmatrix} 0 \\ 1 \\ 0 \end{pmatrix} \right|^2$$

$$= \left| d\sin^2\theta - d\cos^2\theta + (b-a)\sin\theta\cos\theta \right|^2. \tag{19}$$

The polar plots of β-Ga$_2$O$_3$ in this configuration when the analyzer is vertical and horizontal to the incident laser direction are shown in Figs. 3(h) and 3(i), respectively. The practical curvature of the above polar plots may differ in each phonon mode as they depend on the value of a/b/d Raman tensor elements, however the fundamental characteristics remain.

For B$_g$ modes, the ARPRS intensity can be calculated through similar process with B$_g$ Raman tensor elements. To save space of this paper, the calculation part of B$_g$ modes will not be shown here. With the above theoretical calculation, researchers could work out the Raman tensor elements of each of the phonon modes by fitting the ARPRS results with corresponding equations. Kranert et al. have reported ARPRS for A$_g$ and B$_g$ modes as shown in Figs. 4(a) and 4(c), and worked out an entire set of Raman tensor elements [Figs. 4(b) and 4(d)][39]. The spectral position of all 15 Raman active phonon modes and the Raman tensor elements of 13 modes were determined and the Raman tensor elements were found in good agreement with the results from ab-initio calculations.

3.3. Anisotropic photoluminescence properties

The photoluminescence spectra of β-Ga$_2$O$_3$ can be decomposed into three main bands, according to Zhang et al.'s report[37]. The first band at 330 nm is originated from phonon-assisted transition from CBM to self-trapped holes (STH), while the second and third ones at 380 and 400 nm are the sign of free electron detachment by STH at V$_O$ donor positions[41] [Fig. 5(a)]. They also found a strong anisotropic behavior of the PL spectra in β-Ga$_2$O$_3$ as can be seen in Fig. 5(b). In the case of 0° polarization angle [Fig. 5(c)], that is along [001] direction, the PL spectrum can be decomposed into seven bands from UV to yellow. In contrast, there are different peak positions and proportion for the case of 100° polarization direction [Fig. 5(d)], that is along [010] axis. The intensity of the two UV bands are enhanced along the [010] direction, as they are determined by the spatial distribution of STH which are preferable at oxygen sites[42]. Since the O1, O2, O3 sites are aligned in rows along [010] direction as can be seen in Fig. 1(b), the UV luminescence is stronger in 100° polarization. The two blue band, B4 and B5 at 450 and 452 nm, decreased with the polarization angle and disappeared at 100°. The variation of B4 and B5 bands indicates the change of vacancies located at Ga-sites: (V$_{Ga1}$ + V$_{O1}$) and V$_{Ga2}$, which seem to have different electron density distribution and specific dipole moments orientation of recombination transitions more likely closer to the [001] than to the [010] direction.

4. Anisotropic electronic properties

In recent years, β-Ga$_2$O$_3$, as an ultra-wide band gap semiconductor (E_g = 4.9 eV at room temperature) with excellent electrical performance, has gained much attention in preparing high-voltage devices. To better understand the excellent electrical properties of β-Ga$_2$O$_3$, the key parameters of β-Ga$_2$O$_3$ are compared with those of GaN (typical 3rd-generation-semiconductor) and Si (the 1st-generation-semiconductor) materials in Table 2. β-Ga$_2$O$_3$ has better performance in high-voltage electricity than GaN and Si, as its ultra-wide band gap renders the breakdown field strength as high as 8 MV/cm, which is 2.4 times that of GaN and more than 10 times that of Si based devices. Meanwhile, the saturation electron drift velocity of β-Ga$_2$O$_3$ is as high as 2.4×10^7 cm/s, and its Baliga's figure of merit (the key parameter characterizing power device materials) is as high as 3444, which is far higher than the merit value of GaN (846) and SiC (277), the mainstream wide-band gap materials used in power devices at present. Yang et al. reported the vertical structure Schottky diode of Ga$_2$O$_3$:Si with a reverse breakdown voltage of 2300 V[43], and Wong et al. also reported the Si ion implanted Ga$_2$O$_3$ MESFET with a breakdown voltage of 755 V[44]. β-Ga$_2$O$_3$ is proved to be one of the most valuable material for next generation power electronics.

β-Ga$_2$O$_3$ belongs to monoclinic crystal structure with low symmetry. Along the b-axis, Ga atoms are most closely arranged with interplanar spacing of 3.031 Å. Therefore, the electron cloud of Ga 4s orbital overlapped more along b-axis than other directions, resulting in about 18 times higher mobility in this direction than that of c-axis[31]. The anisotropic mobility can be understood by comparing the effective mass along b and c axis. The effect mass can be calculated via

$$\frac{1}{m_{vc}^*} = \frac{1}{m_v^*} + \frac{1}{m_c^*}, \tag{20}$$

$$m^* = \left[\frac{1}{\hbar^2} \left(\frac{\partial^2 E(k)}{\partial k^2} \right) \right]^{-1}, \tag{21}$$

where m^*, m_{vc}^*, m_v^* and m_c^* are the general effective mass, reduced effective mass, valence band effective mass and conduction band effective mass, respectively. $E(k)$, k and $\hbar$ are the electron energy, wave vector and reduced Planck constant. The schematic diagram of the band structure of β-Ga$_2$O$_3$ along wave factor k_y and k_z is shown in Fig. 6(a). The reduced effective mass m_{vc}^* for $E//b$ and $E//c$ is estimated to be $(0.44_{-0.14}^{+0.33})m_0$ and $(1.24_{-0.11}^{+0.15})m_0$, respectively. This is due to the fact that the amount of energy shift experienced by the conduction band, ΔE_C, is identical in all directions even though the curvature of the conduction band is different. On the other hand, the curvature anisotropy of the valence band of the initial states affects the difference of the band gap widening for the orientation of polarization. Since the upper valance band is flatter than the lower one, the m_v^* of the Γ_1^- band along k_z, along c, is heavier than that of the Γ_2^- band along k_y (along b), thus leading to higher electron mobility along b axis.

Carrier mobility is an important parameter to measure the electrical performance of semiconductors, which affects the conductivity, working speed and calorific value of elec-
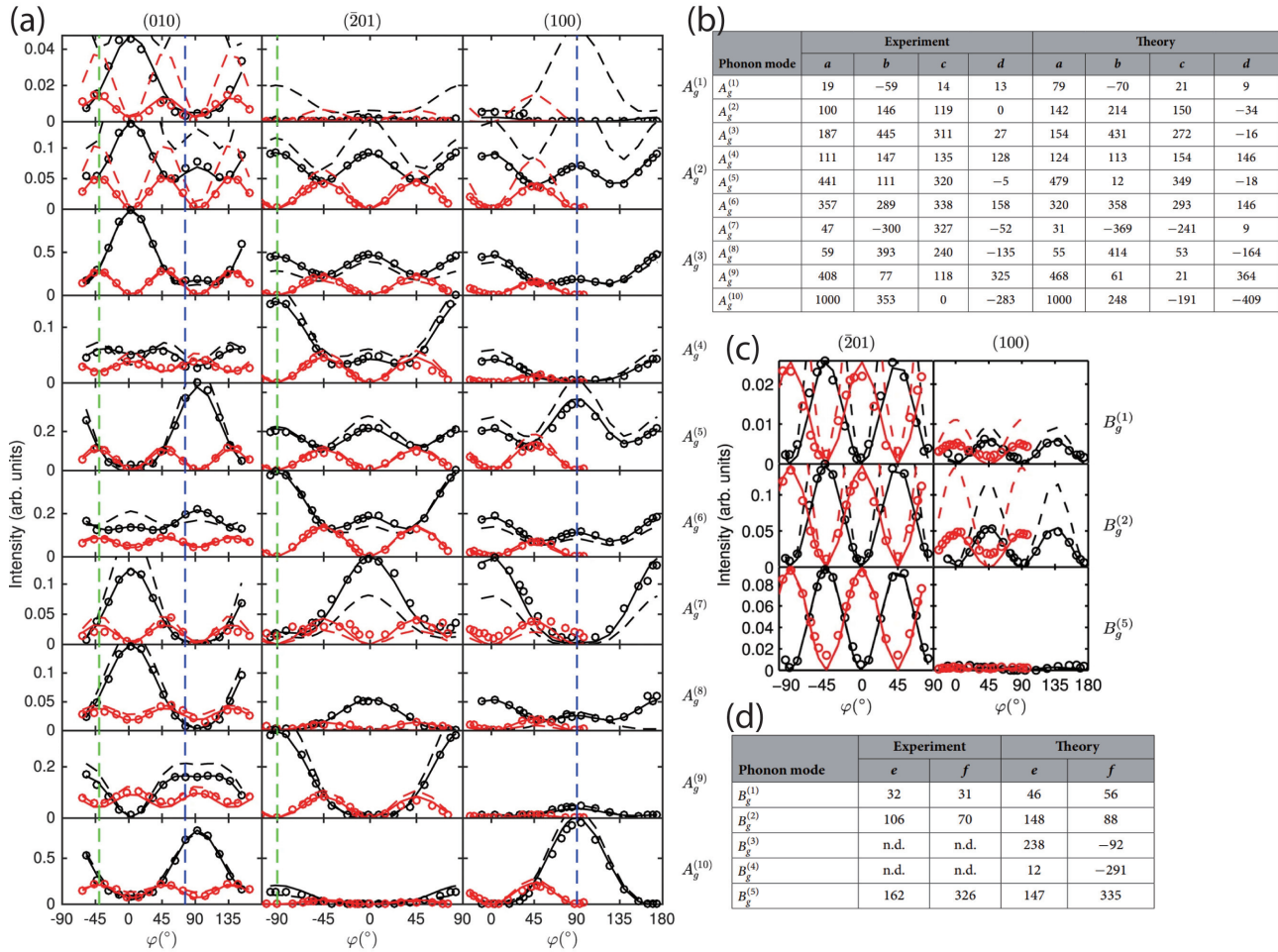
(b)

Phonon mode		Experiment				Theory			
		a	b	c	d	a	b	c	d
$A_g^{(1)}$	$A_g^{(1)}$	19	−59	14	13	79	−70	21	9
	$A_g^{(2)}$	100	146	119	0	142	214	150	−34
	$A_g^{(3)}$	187	445	311	27	154	431	272	−16
$A_g^{(2)}$	$A_g^{(4)}$	111	147	135	128	124	113	154	146
	$A_g^{(5)}$	441	111	320	−5	479	12	349	−18
	$A_g^{(6)}$	357	289	338	158	320	358	293	146
$A_g^{(3)}$	$A_g^{(7)}$	47	−300	327	−52	31	−369	−241	9
	$A_g^{(8)}$	59	393	240	−135	55	414	53	−164
	$A_g^{(9)}$	408	77	118	325	468	61	21	364
	$A_g^{(10)}$	1000	353	0	−283	1000	248	−191	−409

(d)

Phonon mode	Experiment		Theory	
	e	f	e	f
$B_g^{(1)}$	32	31	46	56
$B_g^{(2)}$	106	70	148	88
$B_g^{(3)}$	n.d.	n.d.	238	−92
$B_g^{(4)}$	n.d.	n.d.	12	−291
$B_g^{(5)}$	162	326	147	335

Fig. 4. (Color online) ARPRS results and Raman tensor elements from literature[39]. (a) Raman scattering intensities (circles), model fits (solid lines) and modelled intensities from ab-intio-calculated tensor elements (dashed lines) of the phonon modes with A_g-symmetry of β-Ga$_2$O$_3$ for parallel (black) and cross polarization (red) in dependence on the direction of the (scattered) polarization ϕ. (b) Raman tensor elements of A_g modes. (c) Raman scattering intensities and (d) Raman tensor elements of B_g modes. Copyright 2016 by Nature Publishing Group.

tronic devices. In addition, the primitive cell of β-Ga$_2$O$_3$ is relatively large with 10 atoms, resulting in as many as 30 phonon modes. For comparison: there are 2 atoms in one primitive cell and 6 phonon modes in silicon. The magnitude of phonon modes and low symmetry lattice structure lead to complex phonon-electron coupling in β-Ga$_2$O$_3$[45].

In addition, the electron–phonon coupling would induce different influence on the transport properties of β-Ga$_2$O$_3$ under low and high electric-fields circumstances. The thermal vibration of the lattice would superimpose perturbation on the periodic potential field, however, the perturbation itself is isotropic and will not lead to anisotropic transport of carriers. On the other hand, as the combination of Ga atoms and O atoms in β-Ga$_2$O$_3$ contains some ion-bond components, the vibration of the net dipole moment of the ion-bond will superimpose another electron-phonon interaction. This electron phonon interaction is the coupling of electrons and polarized optical phonons (Bu1 mode), which is essentially a long-range Coulomb interaction and mainly affects the electron transportation in low-electric fields. According to theoretical calculations, it is the anisotropic electron-phonon coupling that leads to the anisotropic mobility of β-Ga$_2$O$_3$ in low electric field[46]. Resulting from the highly anisotropic crystal structure, the Brillouin zone of β-Ga$_2$O$_3$ is anisotropic as well [Fig. 6(b)]. In the case of low-field, the electrons are with low-

energy and mainly occupy the center of Brillouin region near the Γ point. The electronic structure near the Γ point is almost isotropic and will not result in the anisotropic transport of carriers. In the case of high-electric field, the electrons are with high-energy and will locate at the boundary of the Brillouin zone. The high-energy electrons will have a short-range interaction with the Bu6 phonon, whose energy is higher than that of Bu1 phonon'. Since the short-range interaction is a key factor affecting the saturation transportation speed in high-electric field, the transportation properties of electrons of β-Ga$_2$O$_3$ in high electric fields must differ from those in low-electric fields. Despite the lack of experimental report, there are some theoretical studies on the anisotropic mobility on anisotropy performance of β-Ga$_2$O$_3$ power devices. Li et al. included the anisotropic mobility modeling in calculating the electrical performances of β-Ga$_2$O$_3$ (001) power device[47]. The effect of the anisotropic mobility model on the on-state characteristics and reverse recovery are examined, enabling a more accurate prediction of device performance.

The value of electron affinity of β-Ga$_2$O$_3$ from the literature is quite broad, ranging from 2.5 eV[8] to more than 4 eV[7, 48]. The reason can be ascribed, on the one hand, to the effect of different preparation methods, sample morphology and characterization conditions. On the other hand, it is due to the
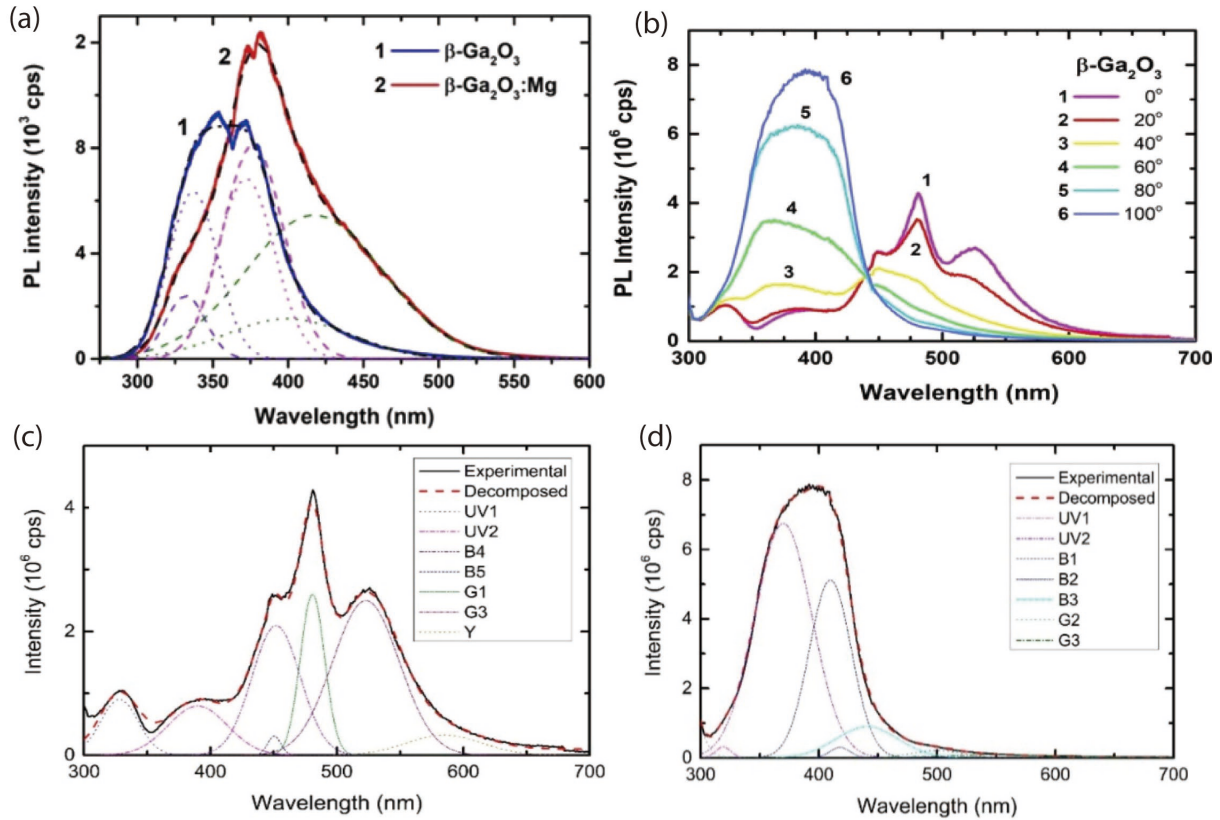
Fig. 5. (Color online) Anisotropic photoluminescence spectra[37]. (a) Unpolarized and (b) polarized photoluminescence spectra of β-Ga$_2$O$_3$. Gaussian spectral components of photoluminescence at (c) 0° and (d) 100° angle of polarizer. Copyright 2021 by Optica Publishing Group.

Table 2. The comparison of electrical properties of β-Ga$_2$O$_3$ with AlN, Diamond, GaN and Si. E_g: banggap energy, E_{br}: breakdown voltage, K: thermal conductivity, Y: Young's modulus.

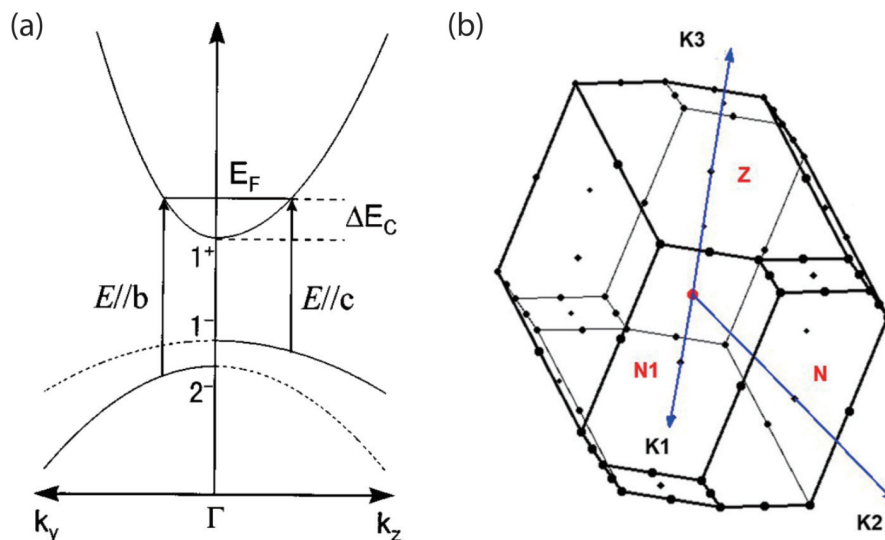| Parameter	E_g (eV)	E_{br} (MV/cm)	Velocity (10^7 cm/s)	K (W/(cm·K))	Y (GPa)
AlN	6.2	17	2.2	2.9	310
Diamond	5.5	10	2.7	10	1100
β-Ga$_2$O$_3$	4.9	8	2.4	0.27	230
GaN	3.4	3.3	2.5	2.1	336
Si	1.12	0.5	1	1.56	130

Fig. 6. (Color online) (a) Schematic diagram of the band structure of β-Ga$_2$O$_3$[31]. Copyright 1997 by AIP publishing. (b) The Brillouin zone of the crystal[45]. Copyright 2016 by AIP publishing.

low symmetry of monoclinic crystal system, which leads to different electron affinity on different crystal planes. However, many reports have not taken the difference of crystal planes into account. According to the metal-semiconductor-contact

Y H Zhang et al.: Anisotropic optical and electric properties of β-gallium oxide

theory, the electron affinity of semiconductor materials affects the contact type and Schottky barrier height (SRH) of electrodes, and the electrode contact performance is extremely important for any device. Therefore, it is also of great significance to study the electrical performance differences between different crystal planes of β-Ga$_2$O$_3$.

5. Applications based on anisotropic properties of β-Ga$_2$O$_3$

5.1. Polarization photodetector

The detection of the polarization state in DUV wavelength is of tremendous importance, particularly, in free space ultraviolet (UV) communication[49]. In our previous work[50], the polarization detectors can be categorized into three types according to their detection mechanisms. The first one is called "dichroism", which means the polarization selectivity is derived from the intrinsic anisotropic optical properties that are related to their anisotropic crystal lattices. Actually, six among the seven crystal systems are expected to be anisotropic, except for cubic crystals[19]. Chen *et al.* reports polarization-sensitive solar-blind photodetectors based on β-Ga$_2$O$_3$ (100) single crystals[35]. They report strong polarized transmittance characteristics [Fig. 2(c)] and light polarization-controlled responsivity for the incident light polarized *E//c* and *E//b*. The schematic diagram of the polarization photodetector is shown in Fig. 7(a), with one (100) single crystal plate above the photodetector device. Since the above single crystal plate is with polarization selectivity like a polarizer, the light that irradiated onto the device varied with the polarization angle of the incident light. The maximum response is sensitive to the polarization angle of incident light, which can be well described by the relation $R(\varphi) = R_{E//c}\sin^2(\varphi) + R_{E//b}\cos^2(\varphi)$ as shown in the inset of Fig. 7(b). Our group first reported polarization photodetector based on single-crystal β-Ga$_2$O$_3$ nanobelts in 2020[50] [Fig. 7(c)]. Different from Chen's report, the working mechanism depends on the intrinsic optical anisotropy. The photoresponsivity [Fig. 7(d)] and response speed [Fig. 7(e)] for *E//*[202] are higher than that for *E//*[020], which was ascribed to the higher absorbance [Fig. 7(f)] for *E//*[202] polarized light.

The second type is referred to as "morphology", as the detection mechanism is related to the attenuated electric field that results from the large dielectric contrast between 1D materials (nanowires, nanorods and nanobelts) and the surrounding environment[51].

Supposing an infinite cylindrical dielectric shell as in Fig. 8(a), with inner diameter a, outer diameter b and dielectric constant of ε, in uniform electric field E_0, the Laplace equation and boundary condition can be written as

$$\nabla^2\phi_1 = 0, \quad r < a, \tag{22}$$

$$\nabla^2\phi_2 = 0, \quad a \leqslant r \leqslant b, \tag{23}$$

$$\nabla^2\phi_3 = 0, \quad r > b, \tag{24}$$

$$\phi_1 = \text{Finit value}, \quad r = 0, \tag{25}$$

$$\phi_1 = \phi_2, \ \varepsilon_0\frac{\partial\phi_1}{\partial\varphi} = \varepsilon\frac{\partial\phi_2}{\partial\varphi}, \quad r = a, \tag{26}$$

$$\phi_2 = \phi_3, \ \varepsilon\frac{\partial\phi_2}{\partial r} = \varepsilon_0\frac{\partial\phi_3}{\partial r}, \quad r = b. \tag{27}$$

Since the electric filed *E* is symmetric on both sides of the x axis, the potential Φ is an even function of angle φ. The potential in different area can be written as

$$\phi_1 = \sum_{n=1}^{\infty} (B_n r^n + D_n r^{-n})\cos n\varphi, \quad r < a, \tag{28}$$

$$\phi_2 = \sum_{n=1}^{\infty} (B'_n r^n + D'_n r^{-n})\cos n\varphi, \quad a \leqslant r \leqslant b, \tag{29}$$

$$\phi_3 = \sum_{n=1}^{\infty} (B''_n r^n + D''_n r^{-n})\cos n\varphi, \quad r > b. \tag{30}$$

By solving the above equations using the Laplace equations and boundary conditions, the express of the potential is solved to be

$$\phi_1 = -\frac{4\varepsilon_r}{(\varepsilon_r + 1)^2 - a^2 b^{-2}(\varepsilon_r - 1)^2} E_0 r\cos\varphi, \quad r < a, \tag{31}$$

$$\phi_2 = \left[-\frac{2(\varepsilon_r + 1)}{(\varepsilon_r + 1)^2 - a^2 b^{-2}(\varepsilon_r - 1)^2} r - \frac{2a^2(\varepsilon_r - 1)}{r(\varepsilon_r + 1)^2 - a^2 b^{-2}(\varepsilon_r - 1)^2} \right]\cos\varphi, \quad a \leqslant r \leqslant b, \tag{32}$$

$$\phi_3 = \left[-E_0 r + \frac{(\varepsilon_r + 1)(\varepsilon_r - 1)(b^2 - a^2)E_0}{r(\varepsilon_r + 1)^2 - a^2 b^{-2}(\varepsilon_r - 1)^2} \right]\cos\varphi, \quad r > b. \tag{33}$$

For one-dimensional infinite cylinder, such as nanowires and nanobelts, the inner diameter *a* is reduced to 0. Eqs. (32) to (33) can be transformed into

$$\phi_2 = -\frac{2}{\varepsilon_r + 1} E_0 r\cos\varphi, \quad r \leqslant b, \tag{34}$$

$$\phi_3 = \left[-E_0 r + \frac{(\varepsilon_r - 1)b^2 E_0}{r(\varepsilon_r + 1)} \right]\cos\varphi, \quad r > b. \tag{35}$$

The electric field *E* can be calculated via $E_2 = -\nabla\phi_2$ to be

$$E_2 = \frac{2}{\varepsilon_r + 1} E_0 = \frac{2\varepsilon_0}{\varepsilon + \varepsilon_0} E_0, \quad r \leqslant b. \tag{36}$$

When the incident field is polarized parallel to the cylinder, the electric field inside the cylinder is not reduced [Fig. 8(c)]. But when polarized perpendicular to the cylinder, the electric field amplitude is attenuated according to Eq. (36)[51], as can be seen in Fig. 8(b). The above derivation process is simplified with infinite model, which does not exist in reality. In practice, nanowires should be as thin as possible to suit the model. Finer 1D materials are preferred to increase the anisotropy. Generally, the diameter of 1D materials
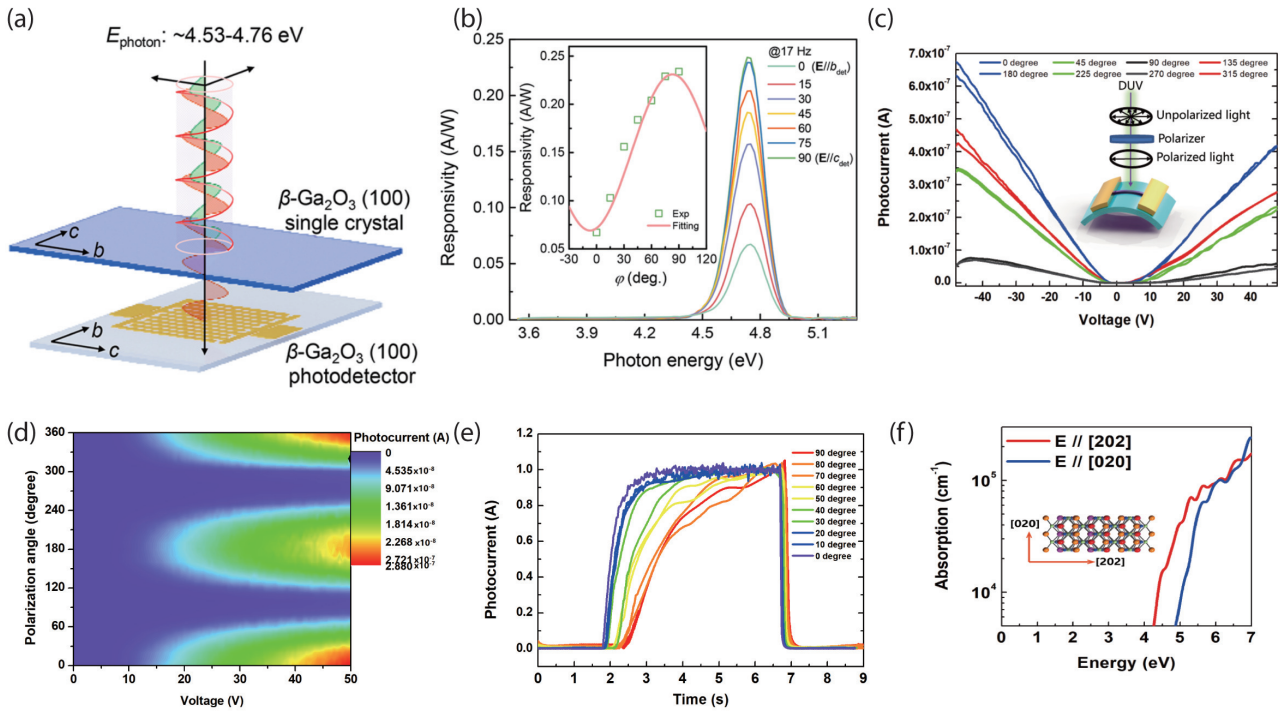
Fig. 7. (Color online) (a) Configuration and (b) the photoresponsivity spectra of the narrow-band polarization detector[35]. Copyright 2019 by American Chemical Society. (c) I–V characteristics and devie configuration, (d) 2D colour map of photocurrent, (e) normalized photoresponse speed and (f) absorption coefficient along [020] and [202] directions[50]. Copyright 2020 by Royal Society of Chemistry.
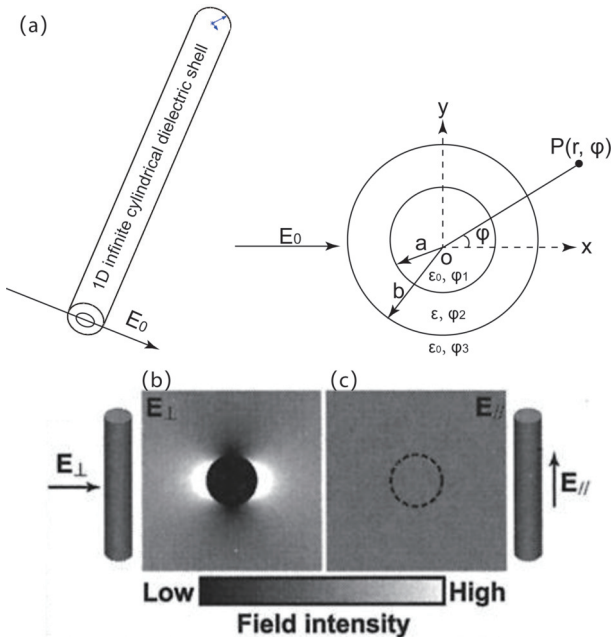

Fig. 8. (a) Infinite dielectric cylindrical shell in uniform external electric field. Field intensities ($|E|^2$) calculated from Maxwell's when external electric field is (b) perpendicular and (c) parallel to the dielectric object[51]. Copyright 2001 by AAAS.

should be much smaller than the excitation wavelength, while the crystallinity is not a key factor. We reported polarization photodetectors based on β-Ga$_2$O$_3$ nanobelts, and ascribed the high anisotropic ratio to the combination of intrinsic dichroism and 1D morphology mechanisms[50].

The third type is referred to as "metal-grid (MG)", which means the detection requires sub-wavelength metal-grids on the active area. Plasmonic meta-surfaces at sub-wavelength

scale, at most one-fifth of the wavelength, are found to function as a polarizing mirror or a polarizer[52, 53]. In addition, sub-wavelength metal grids were integrated with photodetectors to construct focal plane polarization photodetectors[54, 55]. Our group reported enhancement of polarization response in UVA and UVC wavelength by placing sub-wavelength Au grids onto β-Ga$_2$O$_3$ and wurtzite-ZnO materials (Fig. 9)[56]. Au metal-grids, as can be seen in Fig. 9(c), is fabricated with FIB technology and integrated with monoclinic Ga$_2$O$_3$ nanobelts photodetector, bringing about improved polarization rejection ratio from 7.5 to 49 (Fig. 9(d)).

Polarization detection based on monoclinic, triclinic, hexagonal, orthorhombic and tetragonal materials has been summarized in Table 3. β-Ga$_2$O$_3$ based deep-ultraviolet polarization photodetectors emerged since recent years. In Table 3, there are some of the reported works on polarized photodetectors. Most of the works are based on the dichroism properties of the semiconductor material, with less reports based on the attenuated electric field in 1D nanomaterials and few based on metal-grids meta-surfaces. β-Ga$_2$O$_3$ and β-Ga$_x$In$_y$O$_3$ are two kinds of material that have been demonstrated in polarization detection in the UVC range. GaN, ZnO, GeS$_2$ and SnO$_2$ are utilized in the UVA range due to their relatively small bandgap energy. Monoclinic, hexagonal, orthorhombic, tetragonal and triclinic crystal structures are proven to have intrinsic dichroism. Actually, six among the seven crystal systems are expected to be anisotropic, except for the cubic system, which can possess dichroism properties with 1D morphology as well.

5.2. Field-effect transistor

β-Ga$_2$O$_3$ is also a potential candidate for next-generation high-power electronics, as it has superior electrical performance than GaN and SiC. These outstanding properties have

Table 3.   Benchmark of polarization detection reports. (*) represents that the values are calculated by the authors using $\sigma = (I_{peak} - I_{valley})/(I_{peak} + I_{valley})$ according to the data in these references, since they are not directly mentioned. (#) represents that the values are recalculated by the authors using $\sigma = (I_{peak} - I_{valley})/(I_{peak} + I_{valley})$ in order to reach a unified standard, as they were reported as dichroic ratio using I_{peak} / I_{valley}.

Material	Crystal system	Anisotropic plane	Optical bandgap (eV)	Detection wavelength	Material morphology	Anisotropic mechanism	Anisotropy ratio	Ref.
β-Ga$_2$O$_3$	Monoclinic	(−101)	4.8	UVC	3D Nanobelt	Dich. & Morp. & MG	0.96(#)	[56]
β-Ga$_2$O$_3$	Monoclinic	(−101)	4.8	UVC	3D Nanobelt	Dichroism	0.96(#)	[50]
β-Ga$_2$O$_3$	Monoclinic	(100)	4.53-4.76	UVC	3D Bulk	Dichroism	0.53(*)	[35]
β-Ga$_x$In$_y$0$_3$	Monoclinic	(010)	4.4−4.7	UVC	3D Bulk	Dichroism	–	[57]
GeS$_2$	Monoclinic	(001)	3.71	UVA	2D flake	Dichroism	0.36(#)	[58]
SnO$_2$	Tetragonal	(010)	3.6	UVA	3D Microwire	Dichroism	0.39(#)	[59]
MZO/ZnO-MQW	Hexagonal	(11−20)	3.17−3.57	UVA	3D MQW	Dichroism	0.71(#)	[60]
ZnO	Hexagonal	(0001)	3.37	UVA	3D Thin film	MG		[56]
ZnO	Hexagonal	–	3.37	UVA	3D Nanowire	Morphology	0.19(*)	[61]
GaN	Hexagonal	(11−20)	3.4	UVA	3D Thin film	Dichroism	0.76(#)	[62]
GaN	Hexagonal	–	3.4	UVA-UVC	3D Nanowire	Morphology	0.16	[63]
GeSe$_2$	Monoclinic	(001)	2.74	VIS	2D flake	Dichroism	0.55(#)	[64]
GeSe$_2$	Monoclinic	(001)	2.96	VIS	2D flake	Dichroism	0.38(#)	[65]
CsPbI$_3$	Orthorhombic	(100)	2.79	VIS	3D Nanowire	Dich. & Morp.	0.46(#)	[66]
CdSe	Cubic & hexagonal	–	1.79	VIS	3D Nanowire	Morphology	0.13(#)	[67]
ZrS$_3$	Monoclinic	(001)	1.79	VIS	2D nanoribbon	Dichroism	0.27(#)	[68]
ReS$_2$/ReSe$_2$	Triclinic	(001)	1.6/1.3	VIS	2D heterojunction	Dichroism	0.47(*)	[69]
CH$_3$NH$_3$PbI$_3$	Tetragonal	(001)	1.58	VIS	3D Nanowire	Morphology	0.13(#)	[70]
ReS$_2$	Triclinic	(001)	1.5	VIS	2D flake	Dichroism	0.47(*)	[71]
Inp	Cubic	–	1.35	Visible	3D Nanowire	Morphology	0.96	[51]
TiS$_3$	Monoclinic	(001)	1.13	VIS-NIR	2D nanoribbon	Dichroism	0.6(#)	[72]
GeAs$_2$	Orthorhombic	(001)	1	VIS	2D flake	Dichroism	0.33(*)	[73]
TlSe	Tetragonal	(110)	0.73	VIS	2D flake	Dichroism	0.45(#)	[74]
BP	Orthorhombic	(001)	0.3	VIS-NIR	2D flake	Dichroism	0.82(*)	[75]
BP	Orthorhombic	(001)	0.3	VIS-MIR	2D flake	Dichroism	0.63(*)	[76]

led to a large number of reports on various electrical devices based on β-Ga$_2$O$_3$ including field-effect transistors (FETs) and Schottky barrier diodes. Thanks to the high anisotropy of β-Ga$_2$O$_3$ crystal, nanobelts with thickness ranging from 20 to 400 nm could be easily exfoliated from bulk materials and freely transferred to various substrates. This allows β-Ga$_2$O$_3$ nanobelts of equally high-quality as bulk materials and of higher process compatibility. The β-Ga$_2$O$_3$ nanobelts exfoliated from bulk crystal have been used in thin-film transistors since 2013. Hwang *et al*. pioneered high-voltage thin-film transistor based on mechanically exfoliated β-Ga$_2$O$_3$ nanobelts[22], which opens up a new way to fabricate β-Ga$_2$O$_3$ power devices. Mitdank *et al*. also investigated the electrical performance of mechanically exfoliated β-Ga$_2$O$_3$ nanobelts[77]. These works initiated the following research works that involving β-Ga$_2$O$_3$ nanobelts or nanoflakes. Kim *et al*. demonstrated the exfoliation of 2D β-Ga$_2$O$_3$ nanobelts and subsequent processing into a back-gate thin-film transistor on Si/SiO$_2$ substrate[78]. The β-Ga$_2$O$_3$ TFT exhibited an on/off ratio of 10^4 to 10^7 over the operating temperature ranging from 20 to 250 °C.

Despite the exceedingly high electrical performance, however, the low thermal conductivity of β-Ga$_2$O$_3$ has to be considered when fabricating high-power electrical devices. Guo *et al*. reported[79] high anisotropy of thermal conductivities of β-Ga$_2$O$_3$. At room temperature, the thermal conductivities along [010] direction is 27 ± 2.0 W/mK, while it is 10.9 ±

1.0 W/mK along [100] direction. They also ascribed the thermal conductivity at high-temperature to phonon-dominated heat transport as the thermal conductivity follows a ~1/T relationship characteristic. The poor thermal conductivity needs to be improved and the anisotropic thermal conductivity needs intensive study before β-Ga$_2$O$_3$ was fully applied to high power device applications. In addition, the heat management problem related to the low thermal conductivity[80] of β-Ga$_2$O$_3$, can be solved by transferring it to substrates with high thermal conductivity.

6. Conclusion

This review provides a comprehensive overview of anisotropic properties and applications of β-Ga$_2$O$_3$. The anisotropic optical and electrical properties are aroused from the anisotropic crystal structure, which is discussed in detail in Section 2. The normal direction of (100) plane is determined with the Weiss zone law and validated by software model. Due to the highly anisotropic arrangement of atoms, thin nanobelts can be easily exfoliated from the bulk material and transferred to various substrates for the fabrication of electronic and optoelectronic devices. In Section 3, the anisotropic optical properties, including anisotropic bandgap, Raman and luminescence properties, are discussed in detail. Three different ARPRS measurement configurations and Raman intensity, calculated with Raman tensor elements, are reviewed in-depth. The PL intensity is also found different
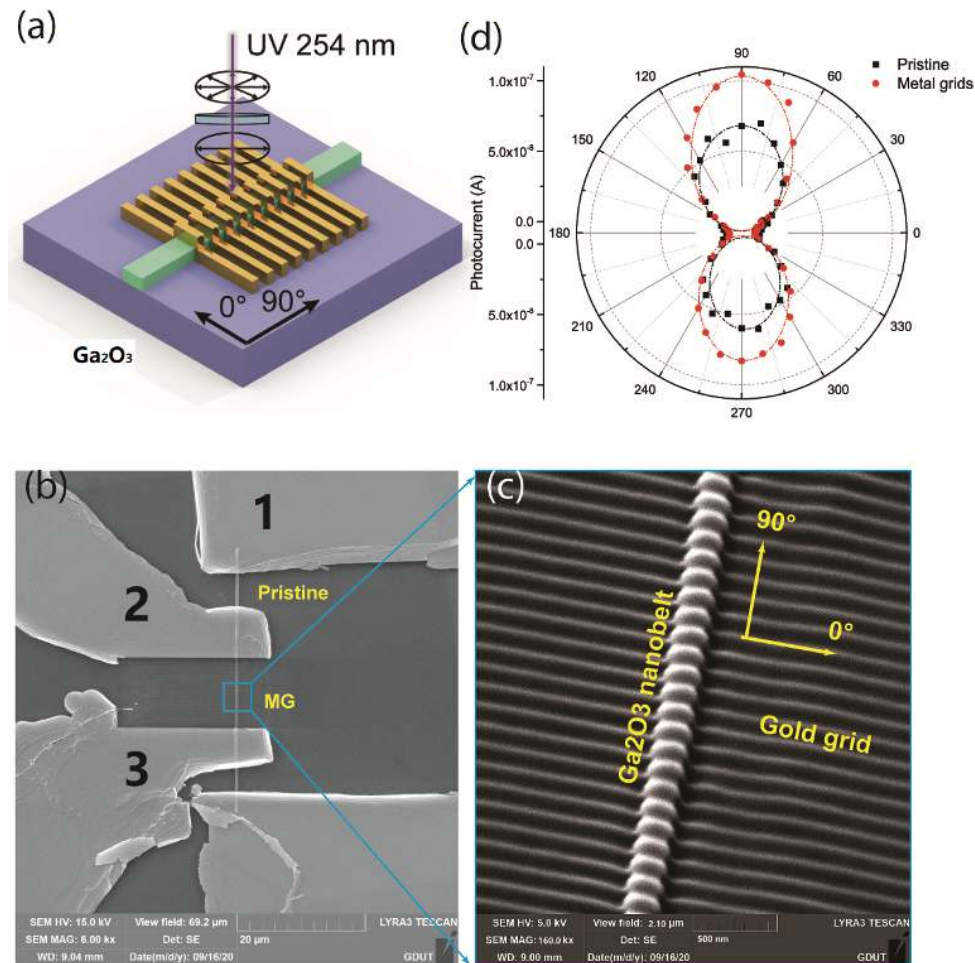
Fig. 9. (Color online) Metal-grid polarized photodetector[56]. (a) Schematics of the device structure. (b) SEM image of β-Ga$_2$O$_3$ device. (c) Enlarged view of the metal grid area. (d) Polarization angle response properties of the pristine and MG β-Ga$_2$O$_3$ devices. Copyright 2021 by Elsevier.

along and perpendicular to the [010] direction. In section 4, the anisotropic mobility value, phonon-electron coupling mechanism and electron affinity are discussed. Finally, polarized photodetector applications are reviewed. Three polarization detection mechanism are presented and discussed in detail. Yet, there is no report on the anisotropy performance of β-Ga$_2$O$_3$ field-effect transistors. So, we discussed the anisotropic thermal conductivity which is of great importance in power electronics instead. Anisotropic properties of β-Ga$_2$O$_3$ would bring about tremendous new research interests and application value. The topic is less explored now, and more research works are required to fully assess and exploit its potential performance and applications.

Acknowledgements

References

[1] Liang H L, Han Z Y, Mei Z X. Recent progress of deep ultraviolet photodetectors using amorphous gallium oxide thin films. Phys Status Solidi A, 2021, 218, 2000339

[2] Kaur D, Kumar M. A strategic review on gallium oxide based deep-ultraviolet photodetectors: Recent progress and future prospects. Adv Optical Mater, 2021, 9, 2002160

[3] Atilgan A, Yildiz A, Harmanci U, et al. β-Ga$_2$O$_3$ nanoflakes/p-Si heterojunction self-powered photodiodes. Mater Today Commun, 2020, 24, 101105

[4] Jian L Y, Lee H Y, Lee C T. Ga$_2$O$_3$-based p-i-n solar blind deep ultraviolet photodetectors. J Mater Sci: Mater Electron, 2019, 30, 8445

[5] Zhao B, Wang F, Chen H Y, et al. An ultrahigh responsivity (9.7 mA W^{-1}) self-powered solar-blind photodetector based on individual ZnO-Ga$_2$O$_3$ heterostructures. Adv Funct Mater, 2017, 27, 1700264

[6] Chen M Z, Ma J G, Li P, et al. Zero-biased deep ultraviolet photodetectors based on graphene/cleaved (100) Ga$_2$O$_3$ heterojunction. Opt Express, 2019, 27, 8717

[7] Cui S J, Mei Z X, Zhang Y H, et al. Room-temperature fabricated amorphous Ga$_2$O$_3$ high-response-speed solar-blind photodetector on rigid and flexible substrates. Adv Opt Mater, 2017, 5, 1700454

[8] Zhao B, Wang F, Chen H, et al. Solar-blind avalanche photodetector based on single ZnO–Ga$_2$O$_3$ core–shell microwire. Nano Lett, 2015, 15, 3988

[9] Han Z Y, Liang H L, Huo W X, et al. Boosted UV photodetection performance in chemically etched amorphous Ga$_2$O$_3$ thin-film transistors. Adv Optical Mater, 2020, 8, 1901833

[10] Qin Y, Long S, He Q, et al. Amorphous gallium oxide-based gate-tunable high-performance thin film phototransistor for solar-blind imaging. Adv Electron Mater, 2019, 5, 1900389

[11] Wang Y, Cui W, Yu J, et al. One-step growth of Amorphous/Crys-

talline Ga_2O_3 phase junctions for high-performance solar-blind photodetection. ACS Appl Mater Interfaces, 2019, 11, 45922

[12] Chi Z Y, Asher J J, Jennings M R, et al. Ga_2O_3 and related ultra-wide bandgap power semiconductor oxides: New energy electronics solutions for CO_2 emission mitigation. Materials, 2022, 15, 1164

[13] Hu Z, Zhou H, Feng Q, et al. Field-plated lateral β-Ga_2O_3 Schottky barrier diode with high reverse blocking voltage of more than 3 kV and high DC power figure-of-merit of 500 MW/cm². IEEE Electron Device Lett, 2018, 39, 1564

[14] Sharma S, Zeng K, Saha S, et al. Field-plated lateral Ga_2O_3 MOSFETs with polymer passivation and 8.03 kV breakdown voltage. IEEE Electron Device Lett, 2020, 41, 836

[15] Sui Y X, Liang H L, Chen Q S, et al. Room-temperature ozone sensing capability of IGZO-decorated amorphous Ga_2O_3 films. ACS Appl Mater Interfaces, 2020, 12, 8929

[16] Liang H, Cui S, Su R, et al. Flexible X-ray detectors based on amorphous Ga_2O_3 thin films. ACS Photonics, 2018, 6, 351

[17] Geller S. Crystal structure of β-Ga_2O_3. J Chem Phys, 1960, 33, 676

[18] Lorenz M R, Woods J F, Gambino R J. Some electrical properties of the semiconductor β-Ga_2O_3. J Phys Chem Solids, 1967, 28, 403

[19] Li L, Han W, Pi L, et al. Emerging in-plane anisotropic two-dimensional materials. InfoMat, 2019, 1, 54

[20] Binet L, Gourier D. Origin of the blue luminescence of β-Ga_2O_3. J Phys Chem Solids, 1998, 59, 1241

[21] Binet L, Gourier D, Minot C. Relation between electron band structure and magnetic bistability of conduction electrons in β-Ga_2O_3. J Solid State Chem, 1994, 113, 420

[22] Hwang W S, Verma A, Peelaers H, et al. High-voltage field effect transistors with wide-bandgap β-Ga_2O_3 nanomembranes. Appl Phys Lett, 2014, 104, 203111

[23] Åhman J, Svensson G, Albertsson J. A reinvestigation of β-gallium oxide. Acta Crystallogr C, 1996, 52, 1336

[24] Oh S, Mastro M A, Tadjer M J, et al. Solar-blind metal-semiconductor-metal photodetectors based on an exfoliated β-Ga_2O_3 Micro-flake. ECS J Solid State Sci Technol, 2017, 6, Q79

[25] Liu X L, Zhang X, Lin M L, et al. Different angle-resolved polarization configurations of Raman spectroscopy: A case on the basal and edge plane of two-dimensional materials. Chin Phys B, 2017, 26, 067802

[26] Li Z, Liu Y, Zhang A, et al. Quasi-two-dimensional β-Ga_2O_3 field effect transistors with large drain current density and low contact resistance via controlled formation of interfacial oxygen vacancies. Nano Res, 2019, 12, 143

[27] Chen J X, Li X X, Huang W, et al. High-energy X-ray radiation effects on the exfoliated quasi-two-dimensional β-Ga_2O_3 nanoflake field-effect transistors. Nanotechnology, 2020, 31, 345206

[28] Bae J, Kim H W, Kang I H, et al. High breakdown voltage quasi-two-dimensional β-Ga_2O_3 field-effect transistors with a boron nitride field plate. Appl Phys Lett, 2018, 112, 122102

[29] Kwon Y, Lee G, Oh S, et al. Tuning the thickness of exfoliated quasi-two-dimensional β-Ga_2O_3 flakes by plasma etching. Appl Phys Lett, 2017, 110, 131901

[30] Kim J, Mastro M A, Tadjer M J, et al. Quasi-two-dimensional h-BN/β-Ga_2O_3 heterostructure metal-insulator-semiconductor field-effect transistor. ACS Appl Mater Interfaces, 2017, 9, 21322

[31] Ueda N, Hosono H, Waseda R, et al. Anisotropy of electrical and optical properties in β-Ga_2O_3 single crystals. Appl Phys Lett, 1997, 71, 933

[32] Varley J B, Weber J R, Janotti A, et al. Oxygen vacancies and donor impurities in β-Ga_2O_3. Appl Phys Lett, 2010, 97, 142106

[33] Ricci F, Boschi F, Baraldi A, et al. Theoretical and experimental investigation of optical absorption anisotropy in β-Ga_2O_3. J Phys:Conden Matter, 2016, 28, 224005

[34] Yamaguchi K. First principles study on electronic structure of β-Ga_2O_3. Solid State Commun, 2004, 131, 739

[35] Chen X, Mu W, Xu Y, et al. Highly narrow-band polarization-sensitive solar-blind photodetectors based on β-Ga_2O_3 single crystals. ACS Appl Mater Interfaces, 2019, 11, 7131

[36] Mu W, Chen X, He G, et al. Anisotropy and in-plane polarization of low-symmetrical β-Ga_2O_3 single crystal in the deep ultraviolet band. Appl Surf Sci, 2020, 527, 146648

[37] Zhang N J, Kislyakov I M, Xia C T, et al. Anisotropic luminescence and third-order electric susceptibility of Mg-doped gallium oxide under the half-bandgap edge. Opt Express, 2021, 29, 18587

[38] Bilbao Crystallographic Server, https://www.cryst.ehu.es/ (accessed August 15, 2022)

[39] Kranert C, Sturm C, Schmidt-Grund R, et al. Raman tensor elements of β-Ga_2O_3. Sci Rep, 2016, 6, 1

[40] Jones R C. A new calculus for the treatment of optical SystemsI description and discussion of the calculus. J Opt Soc Am, 1941, 31, 488

[41] Frodason Y K, Johansen K M, Vines L, et al. Self-trapped hole and impurity-related broad luminescence in β-Ga_2O_3. J Appl Phys, 2020, 127, 075701

[42] Marcinkevičius S, Speck J S. Ultrafast dynamics of hole self-localization in β-Ga_2O_3. Appl Phys Lett, 2020, 116, 132101

[43] Yang J C, Ren F, Tadjer M, et al. 2300V reverse breakdown voltage Ga_2O_3 Schottky rectifiers. ECS J Solid State Sci Technol, 2018, 7, Q92

[44] Wong M H, Sasaki K, Kuramata A, et al. Field-plated Ga_2O_3 MOSFETs with a breakdown voltage of over 750 V. IEEE Electron Device Lett, 2016, 37, 212

[45] Ghosh K, Singisetti U. *Ab initio* calculation of electron-phonon coupling in monoclinic β-Ga_2O_3 crystal. Appl Phys Lett, 2016, 109, 072102

[46] Ghosh K, Singisetti U. Low-field and high-field transport in β-Ga_2O_3. In: Gallium Oxide. Elsevier, 2019

[47] Li Z, Wang Q, Feng C, et al. Simulation study of performance degradation in β-Ga_2O_3 (001) vertical Schottky barrier diodes based on anisotropic mobility modeling. ECS J Solid State Sci Technol, 2021, 10, 055005

[48] Higashiwaki M, Konishi K, Sasaki K, et al. Temperature-dependent capacitance–voltage and current–voltage characteristics of Pt/Ga_2O_3 (001) Schottky barrier diodes fabricated on n⁻–Ga_2O_3 drift layers grown by halide vapor phase epitaxy. Appl Phys Lett, 2016, 108, 133503

[49] Vavoulas A, Sandalidis H G, Chatzidiamantis N D, et al. A survey on ultraviolet C-band (UV-C) communications. IEEE Commun Surv Tutorials, 2019, 21, 2111

[50] Chen Q, Zhang Y H, Zheng T, et al. Polarization detection in deep-ultraviolet light with monoclinic gallium oxide nanobelts. Nanoscale Adv, 2020, 2, 2705

[51] Wang J F, Gudiksen M S, Duan X F, et al. Highly polarized photoluminescence and photodetection from single indium phosphide nanowires. Science, 2001, 293, 1455

[52] Soria E, Gomez-Rodriguez P, Tromas C, et al. Self-assembled, 10 nm-tailored, near infrared plasmonic metasurface acting as broadband omnidirectional polarizing mirror. Adv Opt Mater, 2020, 8, 2000321

[53] Oh S, Lee J H, Lee H J, et al. Polarized ultraviolet emitters with Al wire-grid polarizers fabricated by solvent-assisted nanotransfer process. Nanotechnology, 2019, 31, 045304

[54] Sun D, Feng B, Yang B, et al. Design and fabrication of an InGaAs focal plane array integrated with linear-array polarization grating. Opt Lett, 2020, 45, 1559

[55] Freitas Carvalho F, Augusto de Moraes Cruz C, Costa Marques G, et al. Angular light, polarization and stokes parameters information in a hybrid image sensor with division of focal plane. Sensors, 2020, 20, 3391

[56] Zhang Y H, Wang Z X, Xing F. Enhancement of polarization response in UVA and UVC wavelength with integrated sub-

wavelength metal-grids. Microelectron Eng, 2021, 242/243, 111555

[57] Vasyltsiv V I, Rym Y I, Zakharko Y M. Optical absorption and photoconductivity at the band edge of β-Ga$_{2-x}$In$_x$O$_3$. Phys Stat Sol B, 1996, 195, 653

[58] Yang Y, Liu S C, Wang X, et al. Polarization-sensitive ultraviolet photodetection of anisotropic 2D GeS$_2$. Adv Funct Mater, 2019, 29, 1900411

[59] Li L, Gao W, Chen H Y, et al. Strong anisotropy and piezo-phototronic effect in SnO$_2$ microwires. Adv Electron Mater, 2020, 6, 1901441

[60] Tabares G, Hierro A, Vinter B, et al. Polarization-sensitive Schottky photodiodes based on a-plane ZnO/ZnMgO multiple quantum-wells. Appl Phys Lett, 2011, 99, 071108

[61] Fan Z, Chang P C, Lu J G, et al. Photoluminescence and polarized photodetection of single ZnO nanowires. Appl Phys Lett, 2004, 85, 6128

[62] Rivera C, Pau J L, Muñoz E, et al. Polarization-sensitive ultraviolet photodetectors based on M-plane GaN grown on LiAlO$_2$ substrates. Appl Phys Lett, 2006, 88, 213507

[63] Han S, Jin W, Zhang D H, et al. Photoconduction studies on GaN nanowire transistors under UV and polarized UV illumination. Chem Phys Lett, 2004, 389, 176

[64] Yang Y, Liu S C, Yang W, et al. Air-stable in-plane anisotropic GeSe$_2$ for highly polarization-sensitive photodetection in short wave region. J Am Chem Soc, 2018, 140, 4150

[65] Yan Y, Xiong W, Li S, et al. Direct wide bandgap 2D GeSe$_2$ monolayer toward anisotropic UV photodetection. Adv Optl Mater, 2019, 7, 1900622

[66] Zhou Y, Luo J, Zhao Y, et al. Flexible linearly polarized photodetectors based on all-inorganic perovskite CsPbI$_3$ nanowires. Adv Opt Mater, 2018, 6, 1800679

[67] Singh A, Li X, Protasenko V, et al. Polarization-sensitive nanowire photodetectors based on solution-synthesized CdSe quantum-wire solids. Nano Lett, 2007, 7, 2999

[68] Wang X, Wu K, Blei M, et al. Highly polarized photoelectrical response in vdW ZrS$_3$ nanoribbons. Adv Electron Mater, 2019, 5, 1900419

[69] Liu D, Hong J, Wang X, et al. Diverse atomically sharp interfaces and linear dichroism of 1T'ReS$_2$-ReSe$_2$ lateral p–n heterojunctions. Adv Funct Mater, 2018, 28, 1804696

[70] Gao L, Zeng K, Guo J, et al. Passivated single-crystalline CH$_3$NH$_3$PbI$_3$ nanowire photodetector with high detectivity and polarization sensitivity. Nano Lett, 2016, 16(12), 7446

[71] Liu F, Zheng S, He X, et al. Highly sensitive detection of polarized light using anisotropic 2D ReS$_2$. Adv Funct Mater, 2016, 26, 1169

[72] Liu S, Xiao W, Zhong M, et al. Highly polarization sensitive photodetectors based on quasi-1D titanium trisulfide (TiS$_3$). Nanotechnology, 2018, 29, 184002

[73] Li L, Gong P, Sheng D, et al. Highly in-plane anisotropic 2D GeAs$_2$ for polarization-sensitive photodetection. Adv Mater, 2018, 30, 1804541

[74] Yang S, Hu C, Wu M, et al. In-plane optical anisotropy and linear dichroism in low-symmetry layered TlSe. ACS Nano, 2018, 12, 8798

[75] Hong T, Chamlagain B, Wang T J, et al. Anisotropic photocurrent response at black phosphorus-MoS$_2$ p–n heterojunctions. Nanoscale, 2015, 7, 18537

[76] Yuan H, Liu X, Afshinmanesh F, et al. Polarization-sensitive broadband photodetector using a black phosphorus vertical p–n junction. Nat Nanotechnol, 2015, 10, 707

[77] Mitdank R, Dusari S, Bülow C, et al. Temperature-dependent electrical characterization of exfoliated β-Ga$_2$O$_3$ micro flakes. Phys Status Solidi A, 2014, 211, 543

[78] Kim J, Oh S, Mastro M A, et al. Exfoliated β-Ga$_2$O$_3$ nano-belt field-effect transistors for air-stable high power and high temperature electronics. Phys Chem Chem Phys, 2016, 18, 15760

[79] Guo Z, Verma A, Wu X, et al. Anisotropic thermal conductivity in single crystal β-gallium oxide. Appl Phys Lett, 2015, 106, 111909

[80] Handwerg M, Mitdank R, Galazka Z, et al. Temperature-dependent thermal conductivity in Mg-doped and undoped β-Ga$_2$O$_3$ bulk-crystals. Semicond Sci Technol, 2015, 30, 024006

Yonghui Zhang obtained his PhD degree in condensed matter physics from the Institute of Physics, Chinese Academy of Sciences in 2018. His research interests include flexible transparent electronic, oxide semiconductors and high-voltage devices. Currently, he works in the School of Physics and Optoelectronics Engineering in Shandong University of Technology.

Fei Xing got his PhD degree from Nankai University in optics in 2014. His research interests are the optical properties of graphene-based total internal reflection devices. Now, he works in the School of Physics and Optoelectronic Engineering in Shandong University of Technology, mainly engaged in the application of low-dimensional semiconductor materials and optical devices.